

Nanopore design for exceptional rectification of DNA translocation

Ngan Pham

Uppsala University

Yao Yao

Uppsala University

Chenyu Wen

Uppsala University <https://orcid.org/0000-0003-4395-7905>

Shiyu Li

Uppsala University

Shuangshuang Zeng

Uppsala University <https://orcid.org/0000-0002-7584-6479>

Tomas Nyberg

Uppsala University

Tuan Tran

Uppsala University

Daniel Primetzhofer

Uppsala University

Zhen Zhang

Uppsala University <https://orcid.org/0000-0003-4317-9701>

Shi-Li Zhang (✉ shili.zhang@angstrom.uu.se)

Uppsala University

Article

Keywords: Solid-state nanopores (SSNPs), biotechnology, nanopore design

Posted Date: April 14th, 2021

DOI: <https://doi.org/10.21203/rs.3.rs-382666/v1>

License: © ⓘ This work is licensed under a Creative Commons Attribution 4.0 International License.

[Read Full License](#)

Abstract

Solid-state nanopores (SSNPs) of on-demand shape and size can facilitate desired sensor performance. However, reproducible production of arrayed nanopores of predefined geometry is yet to demonstrate despite of numerous methods explored. Here, bowl-shape SSNPs combining unique properties of ultrathin membrane and tapering geometry are demonstrated. The bowl-SSNP upper opening is 100-120 nm in diameter, with the bottom opening reaching sub-5 nm. Numerical simulation reveals the formation of multiple electroosmotic vortexes (EOVs) originating from distributed surface charge around the pore-bowl. The EOVs determine, collaboratively with electrophoretic force, how nanoscale objects translocate the bowl-SSNPs. Exceptional rectification with higher frequencies, longer duration and larger amplitude is found when DNA strands translocate downwards from the upper large opening than upwards from the bottom smallest restriction. The rectification is a manifestation of the interplay between electrophoresis and electroosmosis. The resourceful silicon nanofabrication technology is ingeniously shown to enable innovative nanopore designs targeting unprecedented sensor applications.

Main Text

Nanopore technology has been intensively investigated for a myriad of applications including biological analysis¹, water desalination^{2,3}, gas separation^{4,5}, selective filtering^{6,7} and power generation^{8,9}. Interest in solid-state nanopores (SSNPs) has grown owing to their versatility in pore design, multiple fabrication schemes available coupled with a rich choice of membrane materials, mechanical and chemical robustness, large-scale manufacturing capability and possibility of on-chip integration with readout and control electronics¹⁰. Various membrane materials have been studied for SSNP generation, including SiN_x ¹¹, SiO_2 ¹² and silicon¹³ that are silicon process compatible; emerging layered single-atom structures such as graphene¹⁴ and MoS_2 ¹⁵ that can facilitate ultrathin nanopores; or glass¹⁶ and polymer^{17,18} that target special routes of fabrication and surface management. Concurrently, a variety of techniques have been employed to manufacture SSNPs, *i.e.*, ion beam^{11,19}, electron beam²⁰, electrical breakdown²¹, electrochemical etching²² and lithography in combination with reactive ion etching²³. Our recently realised truncated-pyramidal nanopores (TPPs) in silicon-on-insulator (SOI) substrate are characterised by a smallest opening (restriction) below 10 nm²⁴. Such a truncated-pyramidal pore shape in combination with the inevitable presence of surface charge on the pore sidewall is predicted by numerical simulation to form an electroosmotic vortex (EOV) inside each TPP upon application of an external electric field. The position, size and strength of the EOV are controllable by the external bias voltage. The EOV can, thus, act as an electric valve to regulate the pathway and speed of the electroosmotic flow, which can account for the experimentally observed rectification of protein translocation in TPPs²⁴.

Both electroosmotic and electrophoretic effects are known^{10,24-27} to affect the transport of nanoscale objects in nanopores. Controllability of the relative contribution of these effects is essential in determining the degree of rectification in transport and in attaining desired sensor performance. To further explore the potential of rectification, this work demonstrates bowl-shape SSNPs (BNPs) and their

unique properties. The concept of BNPs is first validated using numerical simulation, with reference to our previously studied TPPs²⁴. Unlike the BNPs sculptured using focused ion beams^{11,19}, our focus is to study the unique translocation characteristics of the BNPs based on standard silicon technology that supports reproducible and mass production. Both experimentally confirmed and theoretically supported, the bowl-like interior coupled with distributed surface charge on the ultrathin membrane around the smallest restriction of the BNPs give rise to an exceptionally high rectification factor for translocation of heavily charged DNA.

Theory of BNPs

Numerical simulation results for a hemispherical BNP of $d_p=5$ nm at the bottom (diameter of the smallest restriction), $h=55$ nm (thickness of the membrane), $D_p\sim 110$ nm (diameter of the upper opening or the hemisphere) and natural surface charge density²⁸⁻³⁰ of -0.02 C/m² for silicon dioxide (SiO₂) in Fig. 1a clearly show the formation of EOVs. The lower reservoir beneath the smallest restriction is grounded as the potential reference, while a bias voltage is set to the upper reservoir above the large opening. At positive bias $V=+500$ mV, a strong downward electroosmotic flow from the upper reservoir along the surface of the BNP sidewall is directed to a warm-coloured “pear” in the lower reservoir through a narrow channel (width <1 nm). This is complemented by a comparably strong upward flow immediately above the smallest restriction. In addition, a strong upward flow near the edge of the smallest restriction is observed in the lower reservoir. Hence, two vortices, *i.e.*, cyclic flows between the warm and cold colour regions, are formed, with the upper vortex being much stronger in flow rate than the lower one. At negative bias $V=-500$ mV, the position of and flow direction in the vortices remain, although not only the size of the vortices but also the EOF distribution greatly differ due to induced surface charge (ISC). This invariance in position and flow direction of the vortices after reversing the polarity of external bias is of significant implications for DNA translocation shown below. The root cause for the intriguing vortex formation is the surface charge imparity primarily due to the effect of ISC³¹ near the smallest restriction where the membrane remains ultrathin for an extended stretch (Fig. S1b, S2 in Supporting Information). Neglecting the ISC effect would lead to symmetric EOFs about the smallest restriction but with opposite directions at positive and negative biases, as expected (Fig. S1d, S2).

Ionisation of the hydrogen on their phosphate backbone makes DNA molecules heavily negatively charged³². Movement of DNA molecules in a BNP can, therefore, be controlled electrophoretically and significantly modulated electroosmotically^{10,25}. At $V=+500$ mV (Fig. 1a), the electrophoretic force pulls a DNA molecule upwards from the lower reservoir. However, the electroosmotic force below the smallest restriction tends to drag the molecule downwards while that above pushes it upwards. Thus, the electroosmotic force tends to prevent the DNA molecule from entering the BNP from the lower reservoir but drive it out from the BNP (once it is inside) into the upper reservoir. At $V=-500$ mV, the direction of the electrophoretic force is reversed but those of the EOFs in the EOVs remain identical to those at $V=+500$ mV as seen in Fig. 1a. A DNA molecule driven by the electrophoretic force to enter the BNP from the upper reservoir becomes decelerated by the electroosmotic force when it gets close to the smallest restriction. A

long transfer time for the DNA molecule in the BNP is, therefore, anticipated. Similarly, the DNA molecule is accelerated once it moves out into the lower reservoir. The maximum ratio of the electroosmotic force to the opposite electrophoretic force at the same position along the central axis is calculated in Fig. 1b for a simplified assessment using one DNA base pair (bp) segment as a nanoscale object being exerted by the different forces. A rapid growth of the importance of the electroosmotic force with decreasing d_p is evident. The total force, *i.e.*, the sum of electrophoretic and electroosmotic force, exerted on such a DNA segment is shown in Fig. 1c to peak sharply near the smallest restriction. In both cases of $d_p=5$ and 10 nm, the peaks are strongly asymmetrical although the peak heights are largely insensitive to d_p .

The ratio of the total force at $V=-500$ mV to that at $V=+500$ mV on the DNA segment is depicted in Fig. 1d for three BNPs of different d_p . The c-axis, with the position of the smallest restriction as its origin, points to the direction of the electrophoretic force for both positive and negative biases. The total force at $V=-500$ mV is 4-5 times stronger than that at $V=+500$ mV for DNA approaching the smallest restriction of the $d_p=5$ nm BNP, whereas it is about 30% stronger at $V=+500$ mV than that at $V=-500$ mV after it passes through the smallest restriction. Hence, the DNA segment is much more strongly attracted to the smallest restriction from the upper reservoir at negative bias, but it is more easily pulled out from the BNP to the upper reservoir at positive bias. Higher frequency and longer duration for DNA translocation are, then, predicted at negative bias than at positive bias. It is also found in Fig. 1d that the ratio decreases with increasing d_p in the $c<0$ domain and that changing d_p causes little difference in this ratio for driving the DNA segment out from the BNP in the $c>0$ domain.

Fabrication and characterisation of BNPs

Process details for the fabrication of BNPs are summarised graphically in Fig. 2a. The process module employed is local oxidation of silicon (LOCOS) established in standard silicon technology for device insulation³³, *i.e.*, Step 6 in 2a. This module leads to the formation of BNPs in a self-limiting manner in an originally amorphous silicon layer deposited on an oxidised silicon wafer. As the expensive and non-customised SOI wafers are no longer a necessity for making SSNPs, the concept underlying this fabrication process is expected to stimulate design innovations implementable on other substrates than silicon thereby opening up opportunities much beyond today's practice.

The micrographs in Fig. 2b-e present typical data for the BNPs formed with slightly different processes, see **Methods**. While the bottom openings of the BNPs in 2b-c are irregular, those in 2d-e are, respectively, circular ($d_p=65$ nm) and elliptic ($d_{p1}=7$ nm and $d_{p2}=15$ nm) resembling fairly well the shape of the top opening yet of much smaller dimensions. More details supported by experimental data are collected in Fig. S3 (Supporting Information). The irregular bottom openings (2b-c) can be a manifestation of pore formation at the junction of triple silicon crystal grains (Fig. S3). The irregularities can also result from crystal-plan-dependent oxidation and/or local thickness variation of the silicon layer upon crystallisation and grain growth during processing; the latter is evidenced by a roughened surface in Fig. 2f where the cross-section with a 15-degree tilt of a BNP array is shown. The BNP with a concavely curved sidewall is clearly visible as well.

Current-voltage (I - V) characteristic curves of a BNP, measured in electrolytes of different KCl concentration, are depicted in Fig. 2g. Details of the measurement implementation are provided in **Methods**. To extract d_p from nanopore conductance values obtained from the I - V characteristics, a resistance model³⁴ (see detailed derivations in Supporting Note 1) was used to fit the conductance vs. conductivity plot in Fig. 2h. The resultant d_p for this BNP was 4.4 nm with an average surface charge density of $\sigma = -0.017$ C/m². This σ value agrees with the typical charge density of SiO₂ surface²⁸⁻³⁰, as well as with that for the TPPs²⁴. The slight non-linear I - V characteristics result from the asymmetric pore geometry and the inhomogeneous surface charge distribution. The latter is mainly generated by the ISC effect³¹, especially near the tip of the smallest restriction of the BNP.

Translocation of DNA in BNPs

Translocation experiments were first carried out using the $d_p = 4.4$ nm BNP with λ -DNA, see **Methods** for more details. Typical translocation spikes in Fig. 3a could be observed only at negative biases, which can be accounted for by invoking the 4-fold difference in the ratio of total force at negative bias to that at positive bias in Fig. 1d. The observed bias-dependent frequency of translocation events (FTE) is a result of the competition between capture probability and temporary clogging³⁵, compounded by the rapid increase in the ratio of electroosmotic force to electrophoretic force (Fig. S7 in Supporting Information). Frequently observed translocation waveforms displayed in Fig. 3b are characterised by a long low-level blockage followed by a short high-level one falling directly back to the baseline. The 16- μ m-long λ -DNA with 48,502 base pairs soaked in electrolytes can convolute into a loose clump of 1.2 μ m in gyration diameter³⁶. With a persistence length of 35 nm typical for double-stranded DNA³⁷, part of the λ -DNA can dwell in the bowl and occupies a considerable volume in the high-electric-field region of the BNP. This behaviour can render a significant semi-blockade responsible for the long low-level blockage in Fig. 3b. Although the 35-nm persistence length makes bending of the λ -DNA unlikely to fit into the 4.4 nm pore, the λ -DNA can slightly move and rotate until eventually threading through the BNP and causing the short high-level blockage. Lacking such a dynamic mechanism in the absence of a similar bowl below the BNP can explain no observed translocation from the lower reservoir, at positive bias.

The λ -DNA translocation experiments were then implemented on a larger BNP of $d_p = 8$ nm. The pore size was similarly extracted from the conductance data. The amplitude, duration and FTE were extracted from the original records of ionic current traces. The average and spread of these three parameters are compared for different biases in Fig. 3c-e. The amplitude increases significantly with the absolute bias voltage, consistent with other reports³⁸⁻⁴⁰. The amplitude at negative biases is generally higher than that at positive biases. Although their dependency on bias voltage is weak, both duration and FTE are consistently higher at negative biases than at positive biases. The inset of Fig. 3d with typical examples of current traces at -500 mV (blue) and +500 mV (dark red) visualises the remarkable differences in amplitude, duration and FTE.

Fluctuations in current are contributed by translocation spikes, baseline tremble and drift and background noise. The standard deviation in current for the BNP of $d_p=8$ nm is shown to grow with absolute voltage in Fig. 3f and is larger at negative biases than at positive biases. Thus, translocation of λ -DNA at negative biases is more likely to take place and the interaction between the λ -DNA and the nanopore is stronger, since the former leads to more spikes while the latter contributes to an unstable baseline. The outstanding DNA translocation phenomena are closely correlated to the unique structure of and the EOF distribution in the BNPs displayed in Fig. 1. Hence, it is theoretically predicted and experimentally verified that the DNA molecules have a higher probability to translocate at negative biases than at positive biases in the BNPs.

Methods

COMSOL simulation. Numerical simulations based on COMSOL Multiphysics of bowl-shape and truncated conical nanopores with similar dimensions of the experimental BNPs were carried out to gain insights into the nanopore physics. The simulation included the fluid domain and the membrane domain whose relative permittivity was set to 80 and 11.7 for water and silicon, respectively. The ionic movement in an electrolyte was governed by the Nernst–Planck equation, while the electric potential distribution was described by the Poisson equation and the fluid flow was determined by the Navier–Stokes equations. The “Transport of Diluted Species” module (Nernst–Planck equation), the “Electrostatics” module (Poisson equation) and the “Laminar Flow” module (Navier–Stokes equations) were incorporated and fully coupled in our two-dimensional axisymmetric simulation. The mobility of K^+ and Cl^- was $7.0 \times 10^{-8} \text{ m}^2\text{V}^{-1}\text{s}^{-1}$ and $7.2 \times 10^{-8} \text{ m}^2\text{V}^{-1}\text{s}^{-1}$, respectively. The respective diffusion coefficient was then determined through the Einstein relation. With a rotational symmetry along the central axis of the nanopore, the distributions of electric field and electro-osmotic flow were plotted in cross-section along this axis.

Nanopore fabrication. The BNPs were fabricated on ordinary (100) double-side polished silicon wafers 325 μm in thickness. After standard wafer cleaning, the fabrication started by thermal oxidation at 1000 $^\circ\text{C}$ to grow a 150-nm-thick SiO_2 layer. A 55-nm-thick amorphous silicon (a-Si) membrane layer was subsequently deposited at 560 $^\circ\text{C}$, followed by a 20-nm-thick stoichiometric silicon nitride (Si_3N_4) layer at 775 $^\circ\text{C}$, both by means of low-pressure chemical vapour deposition (LPCVD). Although crystallisation of the a-Si layer was inevitable during the Si_3N_4 deposition, this silicon layer is still referred to as a-Si for convenience. The front side of a few selected wafers was subject to ion implantation of arsenic to a dose of $5 \times 10^{15} \text{ cm}^{-2}$ at 20 keV in order to place the dopant peak at the interface between a-Si and Si_3N_4 . Some of the implanted wafers were annealed in nitrogen atmosphere at 850 $^\circ\text{C}$ for 1 hour to electrically activate the dopants, *i.e.*, letting the arsenic atoms replace silicon atoms in the silicon lattice, due to which grain growth in the a-Si layer was expected. After stripping the Si_3N_4 layer in H_3PO_4 solution followed by standard wafer cleaning, a fresh LPCVD- Si_3N_4 layer was deposited again at 775 $^\circ\text{C}$. Circular windows of 60 to 100 nm in diameter were then opened up in the Si_3N_4 layer on the front side by combining electron beam lithography (EBL, Nanobeam Ltd.) with reactive ion etching (RIE). Local oxidation (LOCOS) of the a-

Si exposed in the Si_3N_4 windows was performed in dry oxygen at atmospheric pressure and 850 to 1100 °C for different lengths of time to attain the target LOCOS outcome. It could be noted that LOCOS was developed for electrical insulation of devices in integrated circuits before transistors reached submicron dimensions³³.

Square cavities of side length 150 μm were etched through the silicon substrate and stopped at the 150-nm-thick SiO_2 layer from the rear side. This design was realised using photolithography in combination with deep RIE followed by 30% KOH wet etching at 80 °C. The SiO_2 could provide an excellent etch stop for the KOH etching, because the ratio of KOH etching rate of SiO_2 to that of Si is 1:200. Thus, the a-Si layer on the front side was protected during this step. The large cavities on the rear side were characterised by sloped, instead of vertical, sidewalls at a fixed angle, due to the well-established silicon etch anisotropy in KOH-based solutions, *i.e.*, the preferential chemical reaction of KOH with the (100) planes to the (111) planes of a silicon crystal. Finally, the LOCS SiO_2 grown in the Si_3N_4 windows along with the SiO_2 layer in the large cavities were removed in a buffered hydrofluoric acid. Free-standing silicon membranes with BNPs were obtained.

The formation of bowl-shape nanopores is a natural consequence of the LOCOS process. In the Si_3N_4 windows, the mechanical stress generated during the LOCOS process can be engineered to lead to a self-limiting growth of oxide studs as the nanopore precursors. When the oxide studs are selectively stripped off, nanopores are left behind in the a-Si membrane. By virtue of the LOCOS process, the interior of the nanopores assumes a concave, bowl-look shape. Thus, the self-limiting oxide growth and the subsequent selective oxide removal are key to the formation of highly reproducible BNPs. Although an ordinary silicon wafer is the starting material in this work, other substrates such as quartz or sapphire that can withstand high temperature processing in a standard silicon process line can also be considered. This possibility makes the process extra robust and versatile.

The irregularities in Fig. 2b-c are attributed to the dependence of the oxidation rate on crystal orientation³³ of the crystallised a-Si with crystallites sizing tens of nanometres. It can also result from local thickness variation represented by the surface roughening in Fig. 2f. Rough surfaces can be planarised by means of chemical mechanical polishing, a standard process in modern integrated circuit fabrication. The satisfying result with an ideal circular pore in Fig. 2e points to the paramount importance of dopant activation prior to oxidation, because heavily doped silicon is known to oxidise faster and the rate of oxidation is less dependent on crystal orientation than undoped silicon³³. Prolonging the oxidation time while exploiting the self-limiting nature of the process may also improve the uniformity (Supporting Note 1). The observed formation of nanopores at the triple junction of silicon crystal grains (Fig. S3) can be mitigated via induced grain growth at low temperatures⁴¹ or mediated by metal or metal silicides^{42,43}. Use of tailor-made silicon-on-insulator wafers including lateral overgrowth epitaxy^{44,45} can also be an alternative.

DNA sample preparation. λ -DNA was purchased from Merck KGaA, Darmstadt, Germany. The DNA was used without further purification and dispersed in a 500 mM KCl solution to the concentration of 78 pM (2.5 μ g/ml).

Electrical characterisation and data processing. In all measurements, the bias voltage was set to the upper reservoir on the large opening side of the BNP, while the lower reservoir on the smallest restriction side was grounded, in agreement with the configuration in the COMSOL simulations.

Before measurement, the BNP chips were thoroughly cleaned in a piranha solution with $\text{H}_2\text{SO}_4:\text{H}_2\text{O}=3:1$ (volume ratio) for 30 min and rinsed in deionized water. The chips were then sandwiched by two custom-made polymethyl methacrylate lids with two polydimethylsiloxane O-rings (inner diameter 8 mm) on the two sides for seal. An inlet and an outlet were made in each lid and the KCl solution with certain concentration and λ -DNA dispersions could be injected to the two sides of the nanopore chip. The fluids in the two sides were separated by the chip and the only path of ionic current was through the nanopore. The resistivity of the KCl solution was calibrated using a conductivity meter (Lab 945, Xylem Analytics Germany Sales GmbH & Co. KG). A pair of pseudo Ag/AgCl reference electrodes (2 mm in diameter (Warner Instruments LLC.)) was also mounted in the middle of the lids, which was used to apply a bias voltage and to measure the ionic current. The bias voltage was controlled and the ionic current was recorded using a patch clamp amplifier (Axopatch 200B, Molecular Device Inc.). The ionic current was digitalised by an Axon Digidata 1550A (Molecular Device LLC.) and recorded using the software Axon pCLAMP 10 (Molecular Device LLC.). DNA translocation was detected at a 10 kHz sampling frequency with a 1 kHz four-pole Bessel low-pass filter. The entire experimental set-up was placed inside a Faraday cage to shield against electromagnetic interference.

The translocation spikes on the current traces were extracted automatically by employing a MATLAB program using the function *findpeaks*. The threshold for recognition of a possible spike in the program was set to be eight times the root-mean-squared value of the background noise. The amplitude and duration of each translocation spike were extracted and the translocation frequency was calculated as the reciprocal of the time interval between consecutive events. In addition, the general fluctuation of the current traces was evaluated by their standard deviation. The components in high frequency range (1 kHz- 10 Hz) and low frequency range (<10 Hz) were separated using a filter and the standard deviation was calculated separately.

Electron microscopy for structural analysis. The formation of BNPs was inspected by means of both scanning electron microscopy (SEM – Zeiss LEO 1530) and transmission electron microscopy (TEM – FEI Titan Themis 200). Sample for TEM was prepared using focused ion beam (Zeiss FIB/SEM Crossbeam 550 with Ga ion sculptor gun and Omniprobe 200).

Declarations

Author contributions

S.-L.Z. conceived the idea and supervised the project. N.H.P. manufactured the nanopores, with the assistance of S.Z. and T.N. Y.Y., C.W., S.L. and T.T.T. performed the measurements and simulations. N.H.P., Y.Y., C.W., S.L., D.P., Z.Z. and S.-L.Z. analysed the data. S.-L.Z., N.H.P., Y.Y. and C.W. wrote the manuscript. All authors commented on the manuscript.

Competing interests

The authors declare no competing financial interests.

Acknowledgements

Dr. Si Chen was acknowledged for fruitful discussion about the LOCOS process. This work was financially supported by Stiftelsen Olle Engkvist Byggmästare (194–0646).

Online content

Any methods, additional references, Nature Research reporting summaries, source data, statements of code and data availability and associated accession codes are available at <https://doi.org/???>.

Additional information

Supporting information is available for this paper at <https://doi.org/???>.

Correspondence and requests for materials should be addressed to S.-L.Z.

Reprints and permissions information is available at www.nature.com/reprints.

Publisher's note Springer Nature remains neutral with regard to jurisdictional claims in published maps and institutional affiliations.

Data availability

The data that support the plots within this paper and other findings of this study are available from the corresponding author upon reasonable request.

References

- 1 Miles, B. N., Ivanov, A. P., Wilson, K. A., Doğan, F., Japrun, D. & Edel, J. B. Single molecule sensing with solid-state nanopores: novel materials, methods, and applications. *Chem. Soc. Rev.* **42**, 15–28 (2013).
- 2 O'Hern, S. C., Jang, D., Bose, S., Idrobo, J.-C., Song, Y., Laoui, T., Kong, J. & Karnik, R. Nanofiltration across defect-sealed nanoporous monolayer graphene. *Nano Lett.* **15**, 3254–3260 (2015).

- 3 Amadei, C. A., Montessori, A., Kadow, J. P., Succi, S. & Vecitis, C. D. Role of oxygen functionalities in graphene oxide architectural laminate subnanometer spacing and water transport. *Environ. Sci. Technol.* **51**, 4280–4288 (2017).
- 4 Dong, G., Hou, J., Wang, J., Zhang, Y., Chen, V. & Liu, J. Enhanced CO₂/N₂ separation by porous reduced graphene oxide/pebax mixed matrix membranes. *J. Membr. Sci.* **520**, 860–868 (2016).
- 5 Park, H. B., Kamcev, J., Robeson, L. M., Elimelech, M. & Freeman, B. D. Maximizing the right stuff: The trade-off between membrane permeability and selectivity. *Science* **356**, eaab0530 (2017).
- 6 Walker, M. I., Ubych, K., Saraswat, V., Chalklen, E. A., Braeuninger-Weimer, P., Caneva, S., Weatherup, R. S., Hofmann, S. & Keyser, U. F. Extrinsic cation selectivity of 2D membranes. *ACS Nano* **11**, 1340–1346 (2017).
- 7 Caglar, M., Silkina, I., Brown, B. T., Thorneywork, A. L., Burton, O. J., Babenko, V., Gilbert, S. M., Zettl, A., Hofmann, S. & Keyser, U. F. Tunable anion-selective transport through monolayer graphene and hexagonal boron nitride. *ACS Nano* **14**, 2729–2738 (2020).
- 8 Feng, J., Graf, M., Liu, K., Ovchinnikov, D., Dumcenco, D., Heiranian, M., Nandigana, V., Aluru, N. R., Kis, A. & Radenovic, A. Single-layer MoS₂ nanopores as nanopower generators. *Nature* **536**, 197–200 (2016).
- 9 Zhang, Y., He, Y., Tsutsui, M., Miao, X. S. & Taniguchi, M. Short channel effects on electrokinetic energy conversion in solid-state nanopores. *Sci. Rep.* **7**, 46661/1-14 (2017).
- 10 Wen, C. & Zhang, S.-L. “Fundamentals and potentials of solid-state nanopores: A review”, *J. Phys. D* **54**, 023001/1-34 (2020).
- 11 Li, J., Gershow, M., Stein, D., Brandin, E. & Golovchenko, J. A. DNA molecules and configurations in a solid-state nanopore microscope. *Nat. Mater.* **2**, 611–615 (2003).
- 12 Chang, H., Kosari, F., Andreadakis, G., Alam, M. A., Vasmatzis, G. & Bashir, R. DNA-mediated fluctuations in ionic current through silicon oxide nanopore channels. *Nano Lett.* **4**, 1551–1556 (2004).
- 13 Deng, T., Wang, Y., Chen, Q., Chen, H. & Liu, Z. Massive fabrication of silicon nanopore arrays with tunable shapes. *Appl. Surf. Sci.* **390**, 681–688 (2016).
- 14 Merchant, C. A., Healy, K., Wanunu, M., Ray, V., Peterman, N., Bartel, J., Fischbein, M. D., Venta, K., Luo, Z., Johnson, A. T. C. & Drndić, M. DNA Translocation through graphene nanopores. *Nano Lett.* **10**, 2915–2921 (2010).
- 15 Feng, J., Liu, K., Bulushev, R. D., Khlybov, S., Dumcenco, D., Kis, A. & Radenovic, A. Identification of single nucleotides in MoS₂ nanopores. *Nat. Nanotechnol.* **10**, 1070–1076 (2015).

- 16 Bafna, J. A. & Soni, G. V. Fabrication of low noise borosilicate glass nanopores for single molecule sensing. Ed. M. Wanunu, *PLoS ONE* **11**, e0157399 (2016).
- 17 Arjmandi-Tash, H., Bellunato, A., Wen, C., Olsthoor, R., Scheicher, R., Zhang, S.-L. & Schneider, G.F. Zero-depth interfacial nanopore capillaries. *Adv. Mater.* **30**, 1703602 (2018).
- 18 Choi, J., Lee, C. C. & Park, S. Scalable fabrication of sub-10 nm polymer nanopores for DNA analysis. *Microsyst. Nanoeng.* **5**, 12/1-10 (2019).
- 19 Li, J., Stein, D., McMullan, C., Branton, D., Aziz, M. J. & Golovchenko, J. A. Ion-beam sculpting at nanometre length scales. *Nature* **412**, 166–169 (2001).
- 20 Storm, A. J., Chen, J. H., Ling, X. S., Zandbergen, H. W. & Dekker, C. Fabrication of solid-state nanopores with single-nanometre precision. *Nat. Mater.* **2**, 537–540 (2003).
- 21 Goto, Y., Yanagi, I., Matsui, K., Yokoi, T. & Takeda, K. Integrated solid-state nanopore platform for nanopore fabrication via dielectric breakdown, DNA-speed deceleration and noise reduction. *Sci. Rep.* **6**, 31324/1-8 (2016).
- 22 Feng, J., Liu, K., Graf, M., Lihter, M., Bulushev, R. D., Dumcenco, D., Alexander, D. T. L., Krasnozhan, D., Vuletic, T., Kis, A. & Radenovic, A. Electrochemical reaction in single layer MoS₂: Nanopores opened atom by atom. *Nano Lett.* **15**, 3431–3438 (2015).
- 23 Ahmadi, A. G., Peng, Z., Hesketh P. J. & Nair, S. Wafer-scale process for fabricating arrays of nanopore devices. *J. Micro/Nanolithography, MEMS, and MOEMS* **9**(3), 033011 (2010).
- 24 Zeng, S., Wen, C., Solomon, P., Zhang, S.-L. & Zhang, Z. Rectification of protein translocation in truncated pyramidal nanopores. *Nat. Nanotechnol.* **14**, 1056–1062 (2019).
- 25 Di Fiori, N., Squires, A., Bar, D., Gilboa, T., Moustakas, T.D. & Meller, A. Optoelectronic control of surface charge and translocation dynamics in solid-state nanopores. *Nature Nanotechnol.* **8**, 946–951 (2013).
- 26 Keyser, U. F., Koeleman, B. N., van Dorp, S., Krapf D., Smeets, R. M. M., Lemay, S. G., Dekker, Ny. H. & Dekker, C. Direct force measurements on DNA in a solid-state nanopore. *Nat. Phys.* **2**(7), 473-477 (2006).
- 27 German, S. R., Luo, L., White, H. S. & Mega, T. L. Controlling Nanoparticle Dynamics in Conical Nanopores *J. Phys. Chem. C* **117**, 703–11 (2013)
- 28 Anderson, B. N., Muthukumar, M. & Meller, A. pH Tuning of DNA Translocation Time through Organically Functionalized Nanopores. *ACS Nano* **7**, 1408–1414 (2013).
- 29 Kox, R. et al. Local solid-state modification of nanopore surface charges. *Nanotechnol.* **21**, 335703 (2010).

- 30 Luan, B. & Stolovitzky, G. An electro-hydrodynamics-based model for the ionic conductivity of solid-state nanopores during DNA translocation. *Nanotechnol.* **24**, 195702 (2013).
- 31 Yao, Y., Wen, C., Pham, N. & Zhang, S.-L. On Induced Surface Charge in Solid-State Nanopores. *Langmuir* **36**, 8874-8882 (2020).
- 32 Pabit, S. A., Qiu, X., Lamb J. S., Li L., Meisburger, S. P. & Pollack, L. Both helix topology and counterion distribution contribute to the more effective charge screening in dsRNA compared with dsDNA. *Nucleic Acids Research* **37**(12), 3887–3896 (2009).
- 33 Plummer, J. D., Deal, M. D. & Griffin, P. B. Silicon VLSI Technology – Fundamentals, Practice and Modeling (Prentice Hall, Upper Saddle River, New Jersey, 2000).
- 34 Wen, C., Zhang, Z. & Zhang, S.-L. Physical Model for Rapid and Accurate Determination of Nanopore Size via Conductance Measurement. *ACS Sens.* **2**, 1523–1530 (2017).
- 35 Li, S., Zeng, S., Wen, C., Barbe, L., Tenje, M., Zhang, Z., Hjort, K. & Zhang, S.-L. Dynamics of DNA clogging in hafnium oxide nanopores. *J. Phys. Chem. B* **124**, 11573-11583 (2020).
- 36 Tree, D. R., Muralidhar, A., Doyle, P. S. & Dorfman K. D. Is DNA a Good Model Polymer? *Macromolecules* **46**(20), 8369–8382 (2013).
- 37 Guilbaud, S., Salome, L., Destainville, N., Manghi, M. & Tardin, C. Dependence of DNA Persistence Length on Ionic Strength and Ion Type. *Phys. Rev. Lett.* **122**, 028102 (2019).
- 38 Merchant, C. A., Healy, K., Wanunu, M., Ray, V., Peterman, N., Bartel, J., Fischbein M.I D., Venta, K.y, Luo, Z., A. T. Johnson, C. & Drndic, M. DNA Translocation through Graphene Nanopores. *Nano Lett.* **10**, 2915–2921 (2010).
- 39 Carlsen, A. T., Zahid, O. K., Ruzicka, J., Taylor, E. W. & Hall, A. R. Interpreting the Conductance Blockades of DNA Translocations through Solid-State Nanopores. *ACS Nano* **8**(5), 4754–4760 (2014).
- 40 Larkin, J., Henley, R. Y., Muthukumar, M., Rosenstein, J. K. & Wanunu, M. High-Bandwidth Protein Analysis Using Solid-State Nanopores. *Biophys. J.* **106**, 696–704 (2014).
- 41 Hatalis, M. K. & Greve, D. W. Large grain polycrystalline silicon by low-temperature annealing of low-pressure chemical vapor deposited amorphous silicon films. *J. Appl. Phys.* **63**, 2260-2266 (1988).
- 42 Yuen, C. Y., Poon, M. C., Chan, W. Y. & Qin, M. Investigation of grain formation and growth in nickel-induced lateral crystallization process. *J. Appl. Phys.* **63**, 2691-2695 (2002).
- 43 Wang, H., Chan, M., Jagar, S., Poon, V. M. C., Qin, M., Wang, Y., Ko, P. K. Super thin-film transistor with SOI CMOS performance formed by a novel grain enhancement method, *IEEE Trans. Elec. Dev.* **47**, No. 8, 1580-1586 (2000).

- 44 Friedrich, J., Neudeck, G. Liu, S. Silicon selective and lateral overgrowth epitaxy: Growth and electrical evaluation for devices. *J. de Phys. Coll.* **49**(C4), 71-74 (1988).
- 45 Neudeck, G. W., Pae, S., Denton, J. P. & Su, T.-c. Multiple layers of silicon-on-insulator for nanostructure devices. *J. Vac. Sci. Technol. B* **17**(3), 994-998 (1999).

Figures

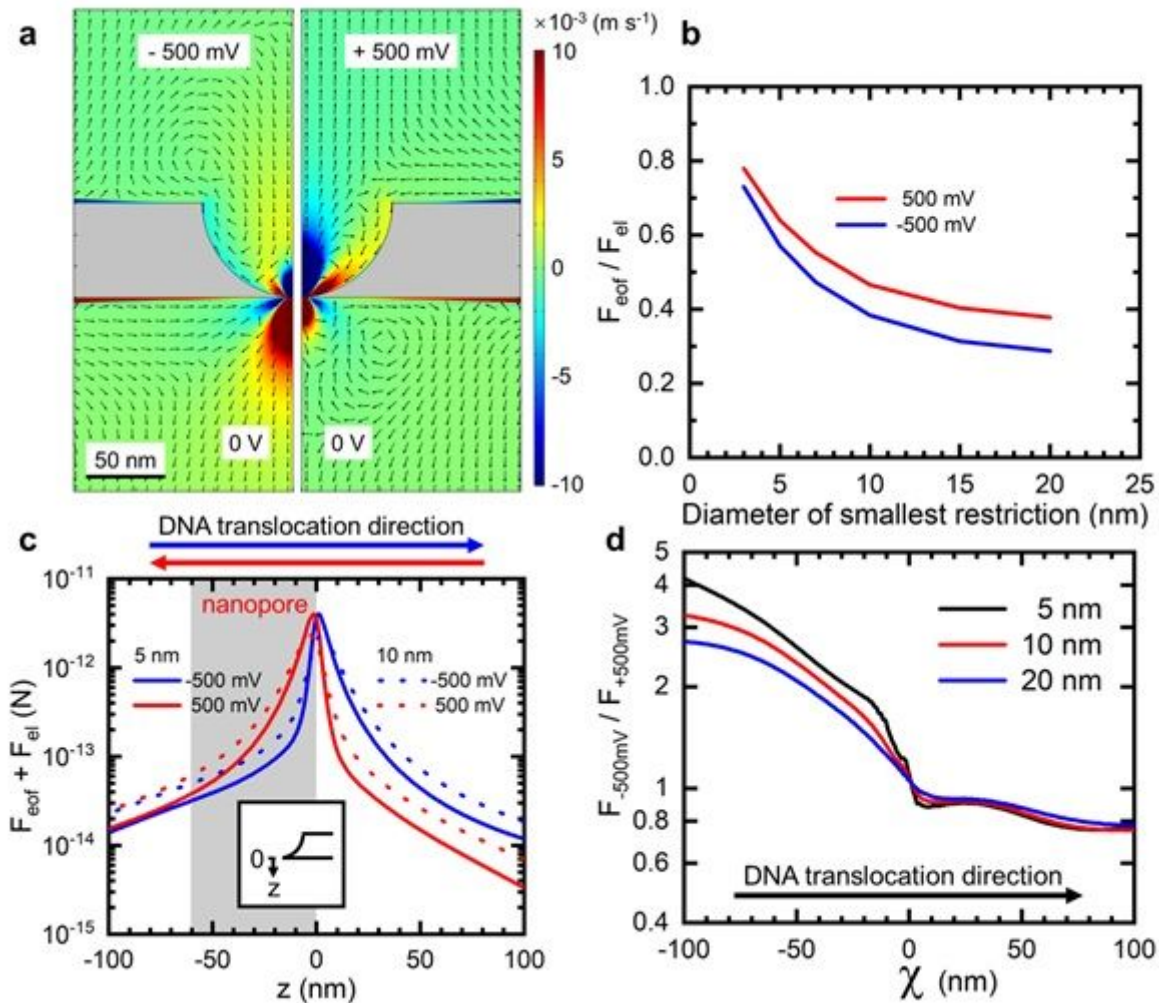


Figure 1

COMSOL simulations for BNPs of $dp=5$ and 10 nm at the bottom (diameter of the smallest restriction that represents the narrowest physical passage of the nanopore), $h=55 \text{ nm}$ (thickness of the membrane) and $Dp \sim 110 \text{ nm}$ (diameter of the upper opening that is equal to the diameter of the hemisphere), in 500 mM KCl and with $\sigma = -0.02 \text{ Cm}^{-2}$ inherent surface charge density. a, Distribution of the EOF velocity at -500 mV (left half) and $+500 \text{ mV}$ (right half) of a BNP of $dp=5 \text{ nm}$ as the diameter of its smallest restriction. Warm colours (red and yellow) indicate downward flows, whereas cold colours (blue and green) present upward flows. The small black arrows indicate the direction of the EOF. b, Dependence on dp of the maximum ratio of the electroosmotic force to the opposite electrophoretic force at the same

position. c, Total force on the DNA molecule along the central axis of BNPs of $d_p=5$ and 10 nm. Inset: the coordinate with the origin lining up with the edge of the smallest constriction and pointing to the lower reservoir. d, Variation of the corresponding ratio of the total force at negative bias to that at positive bias along the c-axis defined as the direction of DNA translocation, i.e., from the upper reservoir to the lower reservoir at negative bias (-500 mV) and from the lower reservoir to the upper reservoir at positive bias (+500 mV).

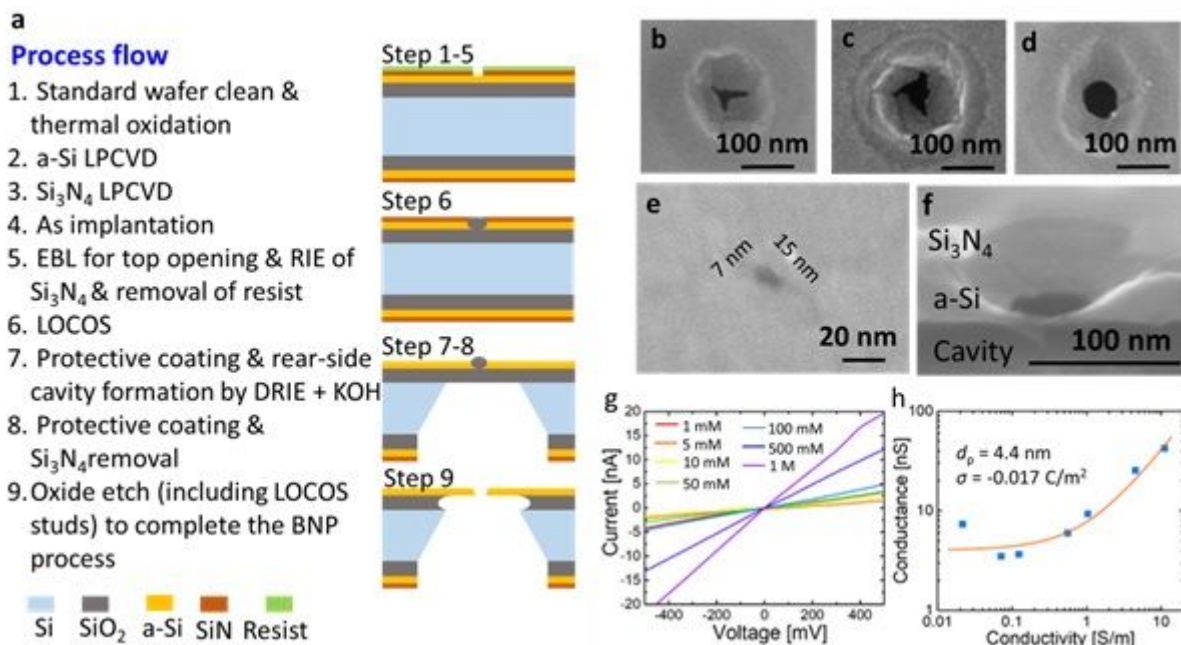


Figure 2

Fabrication and characterisation of BNPs. a, Process details for the formation of BNPs. (Thickness not to scale, shape of bird's beak in the a-Si layer caused by LOCOS not included.) (b-e) Top-view scanning electron microscope (SEM) micrographs showing the bottom opening of the BNPs with: b, Direct oxidation (at 850 °C for 2.5 h) of the crystallised a-Si membrane; c, Oxidation (at 850 °C for 2 h) of the crystallised a-Si layer implanted with a high dose of arsenic; d,e, Oxidation (at 1100 °C for 1 h) of the crystallised a-Si after the implanted arsenic was electrically activated (at 850 °C for 2 h). f, Tilted cross-sectional view of a BNP after removal of the SiO₂ stud clearly showing the bowl-shape sidewall and the bottom opening about 40 nm in diameter. g, Current-voltage characteristic curves of the 4.4 nm BNP in electrolytes of different KCl concentrations. h, Conductance of the 4.4 nm BNP versus conductivity of the electrolytes from which d_p and σ were extracted with the assistance of the nanopore resistance model (Supporting Information).

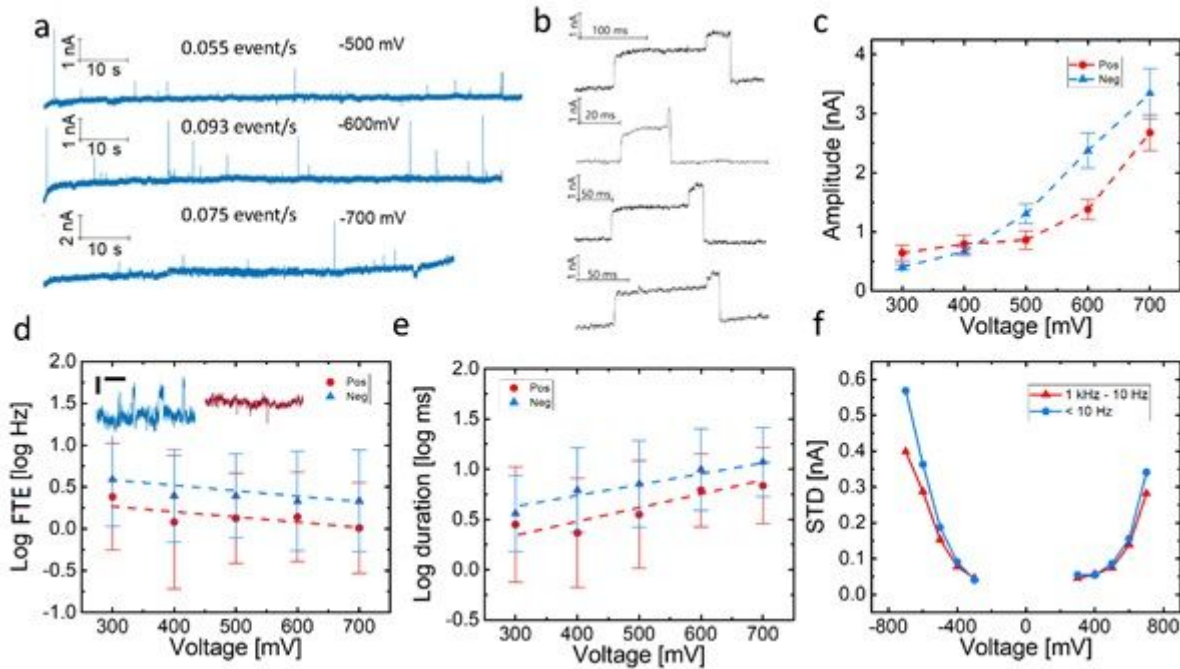


Figure 3

λ -DNA translocation in BNPs. a-b, Translocation of λ -DNA in the 4.4 nm BNP. a, Current traces showing spikes generated by the translocation at different negative biases. b, Examples of the frequently observed translocation waveforms typically showing a long low-blockage period followed by a short high-blockage pulse that falls immediately back to the baseline. c-f, Translocation of DNA in an 8 nm BNP. Dependence on bias of: c, Average amplitude of translocation spikes, d, Mean FTE and e, Average translocation duration. Dots represent average values, while error bars define the spread of corresponding quantities. Dash lines are view guide for a better illustration. Red: positive bias; blue: negative bias. Inset in d: Typical current trace segments showing translocation spikes at -500 mV (blue) and +500 mV (dark red). The horizontal and vertical scale bars are 0.5 s and 0.2 nA, respectively. f, Standard deviation of current traces at different bias in the high frequency range (red, 1 kHz – 10 Hz) and the low frequency range (blue, <10 Hz).

Supplementary Files

This is a list of supplementary files associated with this preprint. Click to download.

- [Nanopore design for exceptional rectification of DNA translocation SI.docx](#)